(Received 11 September 2025, Accepted 31 October 2025, Scheduled 19 December 2025)

Machine Learning-based RCS Prediction for Metasurface-integrated Cavity Structures

Xi Liu[1], Peng Nian[2,*], Yu Zhang[2], Yi Ren[1], Yi-Xin Guo[1], Yang-Chun Gao[3], and Bing Chen[3]

[1]*School of Electronic Engineering, Xidian University, Xi'an 710071, China*
[2]*National Key Laboratory of Digital and Agile Aircraft Design, Chengdu 610091, China*
[3]*China Automotive Engineering Research Institute Co., Ltd, Chongqing 401122, China*

ABSTRACT: Conventional full-wave methods face prohibitive computational costs for far-field scattering optimization of metasurface-integrated cavity structures. To address this limitation, a lightweight residual neural network is introduced within a two-stage scattering prediction framework. This framework effectively mitigates model degradation. The first stage employs shallow convolutional networks to extract local phase-coupling features. The second stage integrates residual layers with fully connected layers to refine cross-scale scattering responses. A compact CNN-ResNet surrogate model is developed for rapid cavity scattering prediction. With only 2.5×10^4 parameters and training on 500 full-wave samples spanning 6.0–16.0 GHz, the model achieves high computational efficiency. The proposed approach directly maps binary phase-coded matrices to far-field electromagnetic characteristics. Extensive validation on a cavity structure across 6.0–16.0 GHz demonstrates excellent accuracy. The per-sample runtime is reduced from hours to milliseconds while maintaining prediction errors below 3 dB. These results confirm the effectiveness of the approach in enabling fast and accurate electromagnetic scattering prediction for complex cavity environments. The approach provides a practical solution for metasurface-integrated cavity optimization.

1. INTRODUCTION

Aircraft electromagnetic stealth performance is quantifiable via radar cross-section (RCS) metrics. Rational RCS minimization directly enhances combat survivability. Electrically large apertures serve as major scattering sources. These include engine intakes, exhaust nozzles, and cockpit openings, etc. Such cavity structures contribute substantially to platform RCS. Therefore, suppressing cavity RCS becomes crucial for enhancing survivability. Full-aspect stealth capability requires these mitigation strategies [1].

Conventional cavity RCS reduction relies on shape optimization [2] and absorptive coatings [3]. These methods demand computationally intensive simulations and iterations, limiting design efficiency. Recent advances in metasurface technology provide an alternative RCS suppression method. Metasurfaces enable flexible electromagnetic wavefront phase manipulation, achieving scattering control through anomalous reflection without structural modifications [4–9]. For example, Paquay et al. [10] implemented a checkerboard configuration combining artificial magnetic conductor (AMC) and perfect electric conductor (PEC) elements. This design utilizes destructive interference for RCS reduction. However, AMC-PEC architectures suffer from inherent narrowband limitations. To overcome this constraint, Ameri et al. [11] developed dual-arrow polarization-converting metasurface (PCM) unit cells. Their design achieved 126% fractional bandwidth RCS reduction under normal incidence from 9–40 GHz, though phase-driven mechanisms remained unexplored. Pan [12] designed a triple-layer stacked coding metasurface providing 3-bit coding in K-band and 1-bit coding in Ka-band, enabling RCS manipulation via frequency-angle cooperative control. However, current metasurface design faces computational bottlenecks. Numerical solutions of Maxwell's equations using the finite element method (FEM) [13] or the finite-difference time-domain (FDTD) [14] algorithm are computationally expensive. These methods rely on point-by-point optimization, severely limiting multi-objective co-design capabilities.

Recent studies have introduced deep learning techniques for metasurface optimization. These methods learn complex nonlinear mappings between metasurface structures and spectral responses. They significantly improve both prediction accuracy and design efficiency. Representative approaches include genetic algorithm-optimized convolutional neural networks (CNN-GA) for rapid amplitude-phase prediction [15], cascaded deep neural network (DNN) paradigms for accelerated inverse design [16], and CNNs achieving millisecond-level spectrum prediction with superior inference speed [17]. However, these methods require large-scale annotated datasets. Performance degrades significantly for electrically large targets such as metasurface-loaded cavities. Furthermore, escalating electromagnetic nonlinearities with problem complexity make accurate modeling increasingly challenging. This necessitates substantial additional training samples, which are typically unavailable in existing industrial databases. Generating new samples through simulation or experimentation introduces substantial time overhead. Consequently, there is a critical need for lightweight deep learning approaches that require smaller sample sizes while maintaining modeling accuracy.

* Corresponding author: Peng Nian (chengxuefeng@stu.xidian.edu.cn).

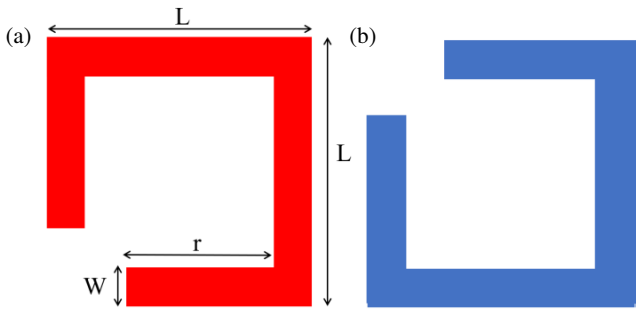

FIGURE 1. Schematic of the fundamental polarization-conversion metasurface unit. (a) "0" unit. (b) "1" unit.

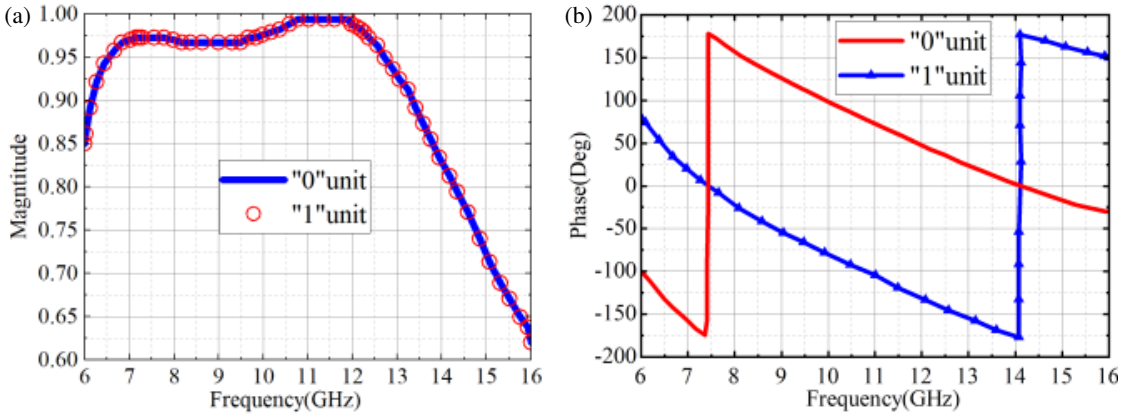

FIGURE 2. Cross-reflection coefficients of "0" and "1" units versus frequency. (a) Magnitude. (b) Phase.

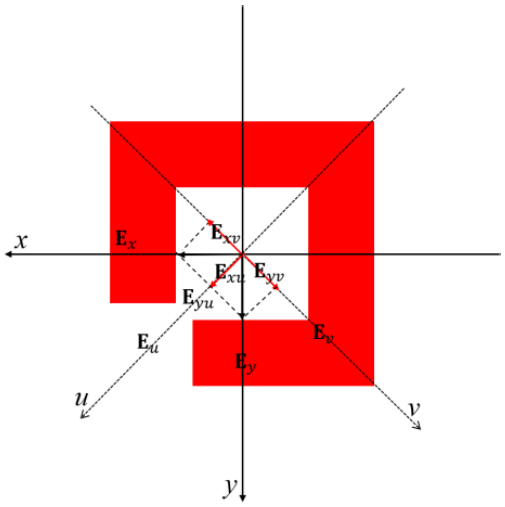

FIGURE 3. Schematic illustrating the operating principle of the fundamental polarization-conversion reflector unit.

To address these challenges, a lightweight two-stage CNN-ResNet framework is proposed for efficient RCS prediction. The first stage utilizes a shallow convolutional network to extract localized coupling features from discrete phase-coding matrices of PCM unit cells. The second stage employs bottleneck residual blocks to refine feature representations. FC layers then perform end-to-end mapping to scattering parameters. This architecture achieves effective convergence with limited training samples. Overfitting is mitigated through early stopping and loss regularization approaches. The lightweight design reduces dependency on large-scale electromagnetic simulation datasets. This work enables accurate scattering prediction at substantially reduced computational cost. Experimental validation on cavity structures confirms the effectiveness of the approach. Prediction errors remain within acceptable engineering tolerance. These results establish the proposed framework as a practical surrogate model for fast and reliable electromagnetic scattering analysis.

The novelty of this work lies in an ultra-lightweight CNN-ResNet surrogate framework. This two-stage architecture maintains robust performance with limited training data. The framework accepts discrete phase distributions of metasurface unit cells as input. This work enables end-to-end prediction of wideband scattering characteristics for cavity-loaded metasurfaces. Consequently, this work supports rapid estimation of scattering characteristics in reconfigurable metasurface-cavity systems. The paper is organized as follows. Section 2 details the design of wideband phase-reconfigurable unit cells and their integration methodology with cavity targets. Section 3 presents the CNN-ResNet algorithm framework. Section 4 validates prediction accuracy through numerical simulations. Section 5 provides concluding remarks.

2. MODEL DESIGN

To validate the proposed algorithm, a metasurface-loaded cavity operating at 6.0–16.0 GHz under VV-polarization is presented. A normally incident plane wave illuminates the cavity

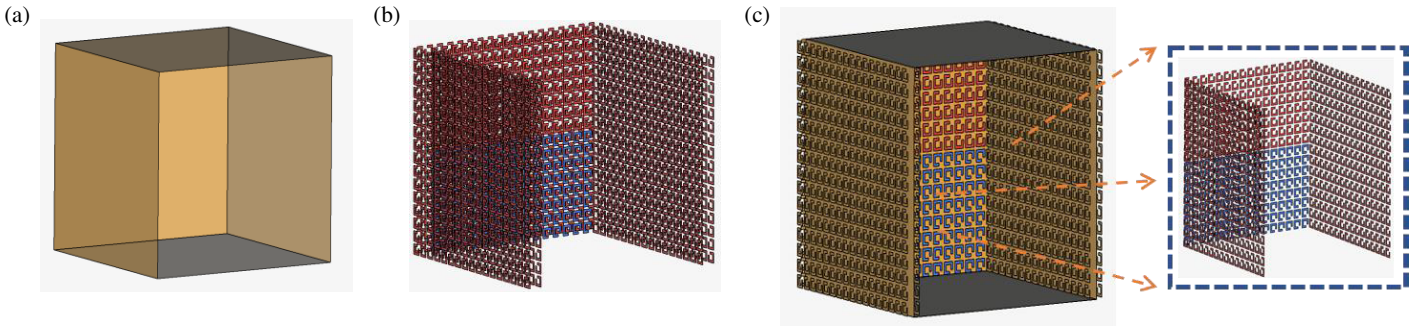

FIGURE 4. Schematic of the metasurface-integrated cavity. (a) The standalone cavity model. (b) The metasurface array loading layer. (c) The cavity model loaded with metasurface unit arrays.

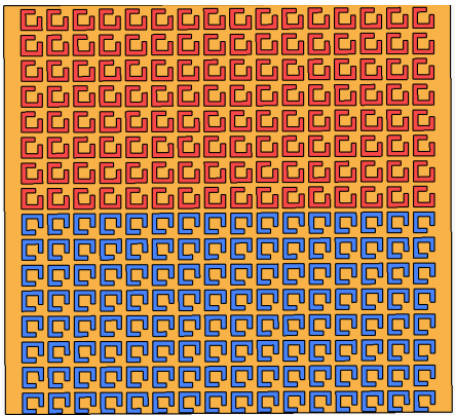

FIGURE 5. Single-surface metasurface arrangement of the control group.

aperture uniformly. Backscattered signals are collected along the same direction in monostatic configuration. The resulting RCS data characterize the cavity-metasurface scattering behavior. It should be noted that this work focuses on rapid prediction of electromagnetic scattering from cavities, not on cavity structure design. Therefore, RCS optimization of the cavity body itself is not addressed in this work.

2.1. Metasurface Unit Design

This work utilizes the polarization-converting reflective metasurface unit from [18] as its fundamental element. This selection balances design efficiency with physical realizability. The unit structure is shown in Fig. 1. A C-shaped split-ring resonator (SRR) forms the basic structure, with dimensions $L = 8.1$ mm, $W = 1.8$ mm, and $r = 5.1$ mm. A 90° rotation of the aperture orientation switches between the "0" state as shown in Fig. 1(a) and "1" state as shown in Fig. 1(b), implementing 1-bit phase coding. Fig. 2 presents the amplitude and phase responses for both states. As shown in Figs. 2(a) and 2(b), the cross-polarized reflection phases maintain approximately 180° difference with equal amplitude across 6.0–16.0 GHz. These results validate the unit's effectiveness for scattering manipulation.

To clarify the physical mechanism behind this phase contrast, we analyze field component phase relationships through polarization conversion principles. As shown in Fig. 3, the original x-y coordinate system is rotated 45° counterclockwise to form the u-v coordinate system. Under y-polarized incidence (incident field $\mathbf{E}_y$), the wave resolves into orthogonal components $\mathbf{E}_{yu}$ and $\mathbf{E}_{yv}$ in the u-v coordinates. The unit behaves as a PMC along the u-direction. This causes the reflected electric field components $\mathbf{E}_{yu}$ and $\mathbf{E}_{xu}$ to maintain identical phase. Conversely, PEC behavior along the v-direction introduces a 180° phase difference between reflected components $\mathbf{E}_{xv}$ and $\mathbf{E}_{yv}$.

Based on electromagnetic field superposition principles, y-polarized incident waves undergo polarization conversion upon reflection. The reflected energy is redirected into the orthogonal x-direction via the metasurface. The Pancharatnam-Berry (PB) geometric phase mechanism introduces an additional phase shift 2α when the metallic pattern rotates by angle α. This rotation inherently generates a 180° phase difference in the cross-polarized reflection channel. The resulting response satisfies the amplitude-phase consistency criterion for 1-bit phase coding. This enables effective manipulation of cavity scattering characteristics.

2.2. Metasurface-Loaded Cavity Design

The "0" and "1" metasurface units are integrated onto a canonical rectangular cavity [19], with dimensions of $160 \times 165.5 \times 171\,\text{mm}^3$ as shown in Fig. 4(a). Metasurface arrays are distributed across three lateral surfaces, excluding the top and bottom faces. Each surface contains an 8×16 unit cell array scaled to match the cavity dimensions. The units are mounted on both inner and outer surfaces of designated faces. A defined separation gap forms the metasurface loading layer, as shown in Fig. 4(b). The cavity is embedded within this assembly to form the metasurface-loaded model, as shown in Fig. 4(c). Magnified views clearly reveal inner-surface arrays consisting of distinct phase-polarization conversion units.

Figure 5 details the metasurface array configuration, which contains separate 8×16 arrays of "0" and "1" units. Each unit is indexed according to its surface position, enabling mapping between cavity scattering responses and phase states. Phase variation in any individual unit modulates the collective electromagnetic control capability through phase-to-RCS mapping. With increasing unit density in inverse design, rapid calculation of cavity electromagnetic properties becomes essential. This

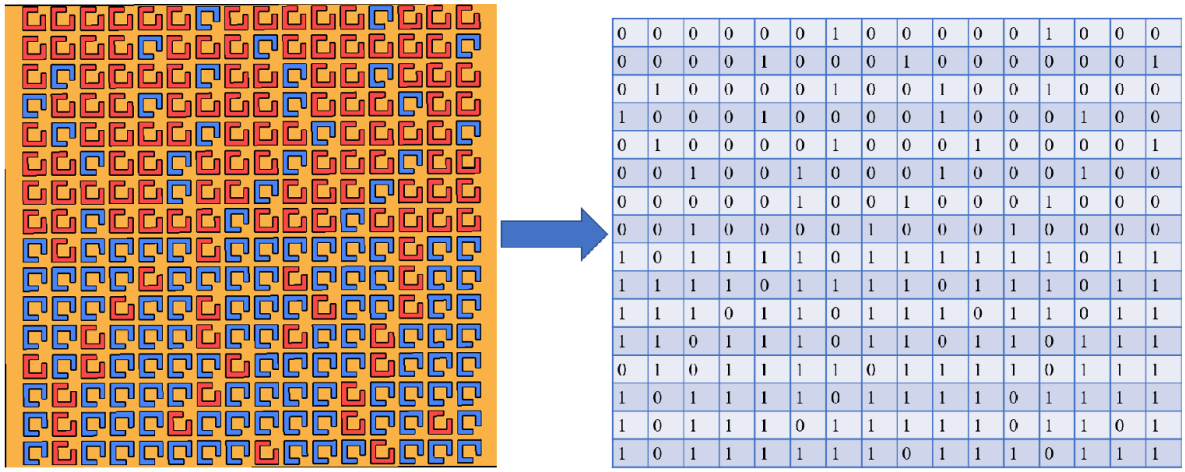

FIGURE 6. Phase-to-matrix mapping of metasurface units.

is particularly important since individual phase adjustments directly alter the overall scattering behavior.

3. CNN-RESNET NETWORK

To achieve rapid cavity RCS prediction, this work proposes a CNN-ResNet architecture. The design aligns with the hierarchical scattering characteristics of metasurface-cavity interactions. Both local phase coupling and global field synthesis collectively determine the RCS response. Convolutional layers effectively extract localized coupling features. Residual connections maintain information flow while capturing global dependencies. This architecture provides a physically interpretable framework for RCS prediction. It also ensures computational efficiency. Accurate prediction is achieved using small-sample cavity RCS data. The overall scheme comprises two main components: dataset acquisition and network architecture.

3.1. Data Preparation

To establish dataset-model mapping, each metasurface unit is represented as a binary element. As shown in Fig. 6, the "0" and "1" states correspond to 0° and 180° cross-polarized reflection phases, respectively. For the cavity's three physical surfaces loaded with metasurfaces, six 16×16 control surfaces are defined. Each surface requires both inner and outer face coverage. The phase arrangement per surface is encoded in matrix $\mathbf{P}_r$ $(r = 1, 2, \ldots, 6)$, with elements $P_r(m, n) \in \{0, 1\}$, $m, n = 1, 2, \ldots, 16$ denoting unit states. The six $\mathbf{P}_r$ matrices are spatially concatenated into a 32×48 global matrix $\mathbf{M}$. This operation preserves individual surface features while incorporating global context.

In practical industrial applications, such datasets are typically obtained through prior simulations and measurements. Industrial users usually possess substantial measurements. Industrial users usually possess substantial simulation and test datasets before implementing AI-assisted design. This study assumes availability of such sample datasets. The commercial EM simulation software FEKO with Multilevel Fast Multipole Method (MLFMM) algorithm is employed for full-wave cavity analysis. Frequency sweeps are performed on $\mathbf{M}$ to generate sample pairs $\{\mathbf{M}, \delta\}$. Here, δ represents the RCS under phase state $\mathbf{M}$. This dataset enables subsequent computational modeling.

The dataset generation accounted for both electromagnetic properties and computational constraints. The configuration space encompasses $2^{32\times48}$ possible metasurface arrangements. Such exponential growth renders exhaustive parameter sweeping impractical. A physics-guided sampling strategy was implemented to ensure physical relevance. The approach utilized row-wise phase control across all six surfaces. Each row was assigned either 0° or 180° phase states. This methodology captures essential scattering behaviors effectively. Representative configurations were synthesized to reflect different interference mechanisms. These include alternating-phase, uniform-phase, and edge-reversed patterns. Physical validity filtering was applied to all generated samples during selection.

The final dataset comprises 500 valid samples. This represents a sampling rate of approximately 5.59×10^{-6} relative to the complete configuration space. Despite its limited size, the dataset provides comprehensive coverage of diverse electromagnetic responses. It maintains both physical consistency and computational efficiency throughout.

3.2. Convolutional Neural Network Architecture

CNNs provide a powerful framework for establishing accurate metasurface topology-to-response mapping. Phase arrangements are encoded into binary matrices (values 0/1), directly corresponding to discrete unit phase states at target frequencies. These matrices intrinsically encode spatial features, leveraging CNNs' hierarchical extraction capability.

3.3. Convolutional Neural Network with Residual Connections

Let the discrete phase 0/1 distribution of metasurface units be defined as the training input, which can be represented by matrix $\mathbf{X}$.

$$\mathbf{X} \in \{0, 1\}^{\mathrm{H}\times\mathrm{W}} \tag{1}$$

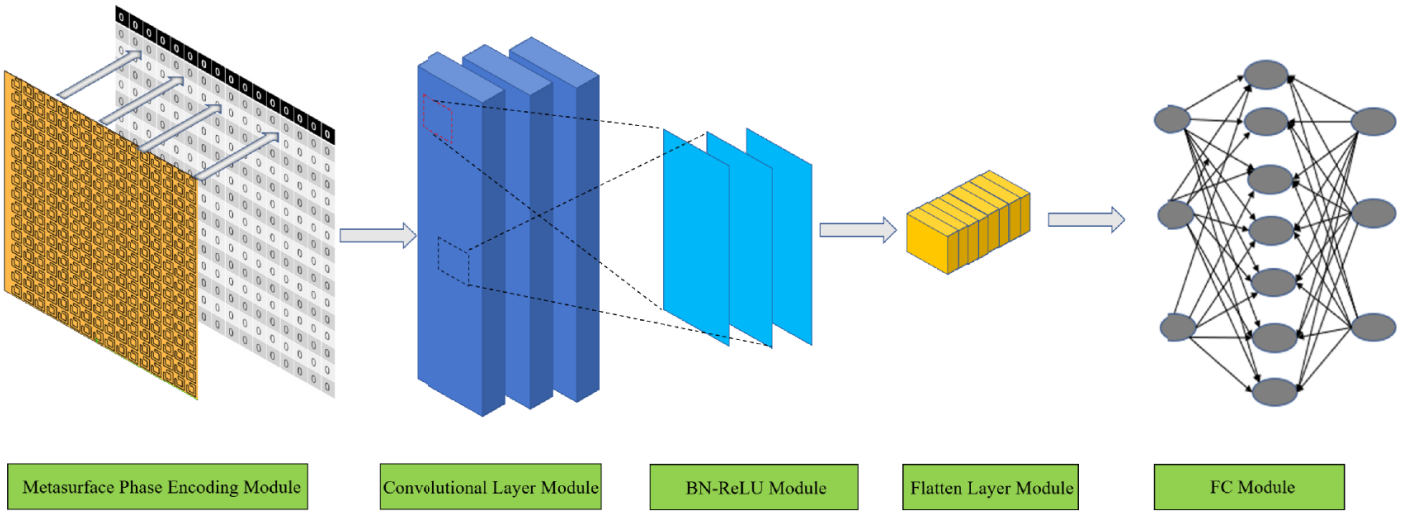

FIGURE 7. Schematic of the CNN network module structure.

TABLE 1. RMSE comparison between CNN and CNN-ResNet networks.

No. Test	RMSE CNN (dB)	RMSE CNN-ResNet (dB)
1	2.415	1.279
2	2.377	0.951
3	2.302	1.102
4	2.352	1.478
5	2.369	1.177
6	2.317	1.305
7	2.274	1.196
8	2.308	1.217
9	2.284	1.228
10	2.244	1.128
Average	2.415	1.206

Phase state "1" corresponds to a 180° phase shift, while "0" represents the 0° reference state. H and W represent the row and column unit counts in the global matrix **M**, respectively. As established in the preceding section, each metasurface unit is modeled using 0/1 values in the matrix. We set $H = 32$ and $W = 48$, resulting in a discrete 32×48 binary input matrix.

$$\mathbf{X}^{(0)} \in R^{\mathrm{H}\times\mathrm{W}\times 1} \tag{2}$$

To differentiate layer inputs/outputs, **X** denotes each network layer's data flow. Superscript 0 marks the initial input layer, labeled as $\mathbf{X}^{(0)}$. Subsequent layers inherit this indexing convention. CNN layers inherently process three-dimensional data. Here, a single-channel input tensor is introduced. This tensor encodes metasurface-loaded cavity information. This tensor serves as the CNN's primary input. Fig. 7 illustrates the convolutional neural network architecture. Eq. (2) mathematically defines the metasurface phase coding module. The CNN then performs local feature extraction. The CNN learns hierarchical representations from the input data. The phase-encoded input data is processed by the convolutional layer depicted in Fig. 7.

The convolutional module performs local receptive field feature extraction, achieving dimensionality reduction of the input data. The processed outputs are then fed into the batch normalization (BN) layer. Subsequently, the data flows through the rectified linear unit activation layer. The combined BN-ReLU module performs feature refinement while enhancing nonlinear representation capability. This processing pipeline is shown in Fig. 7 through the convolution module and BN-ReLU module.

$$\mathbf{X}^{(1)} = \mathrm{ReLU}\left[\mathrm{BN}\left(W_{\mathrm{init}} * \mathbf{X}^{(0)}\right)\right], \quad W_{\mathrm{init}} \in R^{3\times3\times1\times2} \tag{3}$$

As defined in Eq. (3), the feature extraction output $\mathbf{X}^{(1)}$ is obtained by processing the input data through both convolutional and BN-ReLU operations. The convolutional operation employs a 3×3 kernel size, where $W_{init} \in R^{3\times3\times1\times2}$ denotes a two-channel convolution kernel with 3×3 dimensions. The convolutional kernel performs feature detection, accompanied by feature compression during this stage. The BN layer maintains gradient magnitudes within effective ranges, thereby reducing overfitting risks in small-scale datasets. Meanwhile, the ReLU activation layer enhances nonlinear modeling capability while mitigating gradient vanishing issues.

Subsequently, $\mathbf{X}^{(1)}$ is fed into the subsequent flatten layer and FC layer of the CNN network, as shown in the last two modules of Fig. 7.

$$\begin{aligned} \mathbf{X}_{\mathrm{flat}} &= \mathrm{vec}\left(\mathbf{X}^{(1)}\right) \\ \mathbf{X}^{(2)} &= \mathbf{W} * \mathbf{X}_{\mathrm{flat}} + \mathbf{b} \end{aligned} \tag{4}$$

In Eq. (4),vec(•) represents the row-wise flattening operation applied to the input data. Multidimensional feature maps are transformed into one-dimensional vectors. This operation facilitates subsequent processing by the FC layer. The flattened 1D feature vector is then mapped to the output space through the FC layer. High-dimensional nonlinear combinations are achieved. **W** and **b** in Eq. (4) represent the layer's weight matrix and bias vector, respectively.

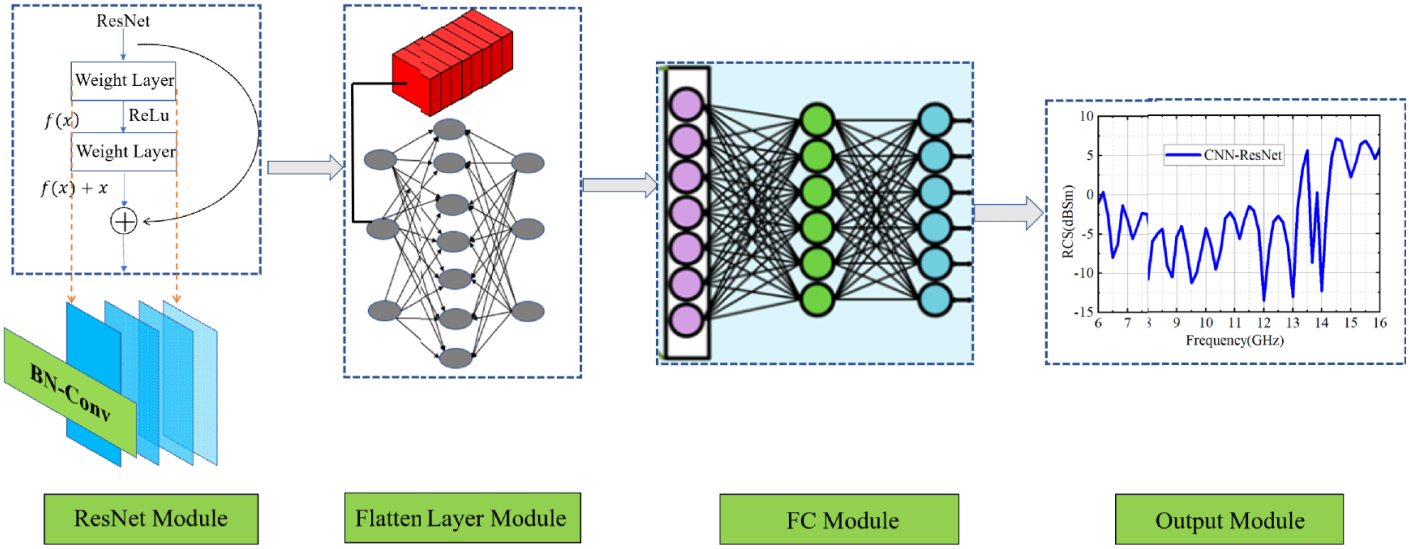

FIGURE 8. Residual network module.

After CNN layer processing, the output data $\mathbf{X}^{(2)}$ is delivered as input to ResNet's compact residual block for processing. Fig. 8 illustrates this architecture through subsequent residual network modules. Each module contains four cascaded components: ResNet module, flatten layer, FC layer, and output layer. The ResNet block implements two convolutional layers followed by a BN-ReLU activation module. Processed features first pass through the flatten layer for dimensionality reduction to 1D vectors. These vectors then enter the FC layer to learn highorder nonlinear mappings. Finally, the output layer generates predictions of electromagnetic scattering characteristics. The ResNet block employs convolutional layers with identical kernel size but increased filter counts relative to the base CNN, enhancing the capture of complex phase variations in the scattering module. A value of 4 is selected for numF in Eq. (5) to balance model complexity and overfitting risks under constrained training data.

$$\begin{aligned}\mathbf{X}^{(3)} =& \text{ReLU}\left[\text{BN}\left(W_{\text{ResNet}} * \mathbf{X}^{(2)}\right)\right], \\ & W_{\text{ResNet}} \in R^{3\times 3\times \text{numF}\times \text{numF}} \\ \mathbf{X}^{(4)} =& \text{BN}\left(W_{\text{ResNet}} * \mathbf{X}^{(3)}\right), \\ & W_{\text{ResNet}} \in R^{3\times 3\times \text{numF}\times \text{numF}}\end{aligned} \tag{5}$$

The residual block in Eq. (5) adopts a structure similar to the CNN module but uses different convolution kernel sizes. The parameter numF specifies the number of filters. Input features are processed sequentially through two convolutional layers. The first layer extracts localized phase features. The second layer recombines these features to refine their representation. This design captures global scattering effects resulting from local phase perturbations through superposition. BN is applied to the output. This stabilizes feature distributions before the residual connection.

$$\mathbf{X}^{(5)} = \text{ReLU}\left(\mathbf{X}^{(4)} + \mathbf{X}^{(2)}\right) \tag{6}$$

As shown in Eq. (6), residual addition sums the convolutional output with the original input. This operation occurs after feature extraction. The network learns incremental scattering changes caused by localized metasurface phase variations. These learned modifications are directly incorporated into the initial phase state's response. This approach significantly reduces the number of parameters. It also mitigates overfitting compared to direct learning methods.

$$\begin{aligned}\mathbf{X}^{2}_{\text{flat}} &= \text{vec}\left(\mathbf{X}^{(5)}\right) \\ \mathbf{X}^{(6)} &= \mathbf{W}^{2} * \mathbf{X}^{2}_{\text{flat}} + \mathbf{b}_2\end{aligned} \tag{7}$$

After the residual block, as shown in Fig. 8, the output $\mathbf{X}^{(5)}$ is processed similarly to the CNN layer. $\mathbf{X}^{(5)}$ is passed through a flatten layer and FC layer. High-dimensional data is reduced to low dimensions via flattening. Subsequent high-dimensional spatial mapping is then performed, as shown in Eq. (7). To distinguish from the weight matrix and bias vector in the CNN layer, superscript notation is utilized for differentiation.

$$\mathbf{X}^{(8)} = \text{ReLU}\left(\mathbf{W}^{3} * \mathbf{X}^{(6)} + \mathbf{b}^{3}\right) \tag{8}$$

In Eq. (8), the processed data $\mathbf{X}^{(6)}$ from ResNet and preprocessing modules is fed into the final FC layer. The output $\mathbf{X}^{(8)}$ is then obtained. This FC layer uses uniquely superscripted weight parameters. A preceding ReLU activation enhances nonlinear mapping capability. The layer functions as the decision component, integrating spatially distributed features to construct a global RCS-structure mapping. It transforms abstract features into RCS curves across discrete frequency points. This completes the end-to-end pipeline from phase-plane data to far-field scattering outputs.

The CNN-ResNet framework delivers optimal accuracy, efficiency, and lightweight design for metasurface-to-cavity RCS prediction. Multiple alternative architectures were evaluated but exhibited significant limitations.

U-Net [20] introduces structural redundancy through decoder paths and skip connections. These components benefit

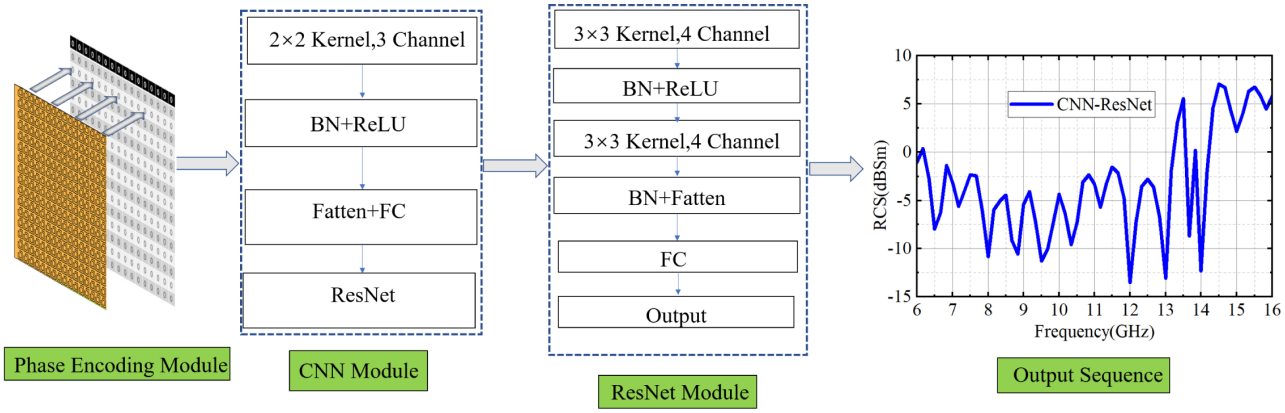

FIGURE 9. Overall network module.

image reconstruction tasks but prove unnecessary for phase-to-RCS mapping. The resulting redundancy increases parameter count and inference latency without improving interpretability.

Transformer models [21] flatten 2D phase matrices into 1D sequences. This process disrupts spatial adjacency relationships that are crucial for electromagnetic coupling analysis. Their self-attention mechanisms also demand substantial computational resources, hindering real-time deployment.

DenseNet [22] achieves strong performance with large datasets but tends to overfit when training samples are limited. Its computational requirements remain excessive for small-data scenarios like the present study.

In comparison, CNN-ResNet preserves local feature integrity through 3×3 convolutions. Residual connections enable effective global feature propagation while maintaining spatial relationships. This architecture ensures stable training convergence and robust generalization capability.

The framework aligns effectively with both electromagnetic modeling requirements and practical computational constraints. CNN-ResNet therefore provides an optimal balance for accurate and efficient RCS prediction in metasurface-loaded cavity applications.

Figure 9 illustrates the CNN-ResNet architecture comprising four core modules: input, CNN network, ResNet network, and output. Polarization-conversion metasurface data is preprocessed by the input module. Metasurface units are phase-encoded spatially. The data are converted to CNN compatible tensors. The CNN network extracts local and global spatial features from structural matrices via convolutional layers. The ResNet network captures global scattering patterns induced by partial phase modifications, enhancing model capacity. Flattened features are mapped to high-dimensional representations. FC layers are used to establish an end-to-end phase coding-to-scattering mapping. Scattering response sequences are efficiently computed. Target electromagnetic structures are processed.

4. NUMERICAL RESULTS

The proposed framework validates cavity scattering predictions. The metasurface-loaded structure in Fig. 4 is utilized. Rapid RCS prediction is enabled with limited training data. Local structural features are extracted by a shallow convolutional backbone. Overfitting is reduced through this design. Vanishing gradients are mitigated by ResNet. Convergence stability is improved. Non-negative constraints are enforced on phase-to-RCS mappings. This is implemented at the output layer. Physical consistency is ensured.

A control group test is established before network construction. Electromagnetic scattering manipulation is evaluated. Metasurface unit phases on the cavity target mode are examined. As shown in Fig. 10, the Original curve represents the RCS sequence of the cavity without manipulation. The Modified curve represents the manipulated electromagnetic scattering characteristics after partial metasurface phase alterations. The distinction between models is attributed to phase inversion. Specific metasurface units are inverted on one cavity surface. This is illustrated in Fig. 10's thumbnail. All metasurface units on the modified surface are transformed. Phase states are changed from 0° to 180°. Units on other surfaces remain unchanged. RCS variations are demonstrated across 6.0–16.0 GHz. These variations are induced by phase modifications. Cavity electromagnetic scattering characteristics are confirmed to be manipulated. Metasurface unit phase adjustments are verified as the control mechanism. Next, the deep learning network architecture is defined.

Training datasets are constructed by partitioning the array into sub-regions. Corresponding sections across different configurations are merged. Phase modulation is applied per sub-region block to assemble the datasets. The root mean square error (RMSE) is selected as the evaluation metric. It quantifies prediction accuracy during inference as:

$$\mathrm{RMSE} = \sqrt{\frac{1}{n}\sum_{i=1}^{n}(y_i - \hat{y}_i)^2} \tag{9}$$

where y_i and $\hat{y}_i$ represent the true and predicted RCS sequences, respectively. Parameter n denotes the number of frequency sampling points.

In practical applications, AI-assisted electromagnetic design typically utilizes pre-existing industrial datasets. These datasets are generally accumulated during prior development phases through extensive simulation and testing.

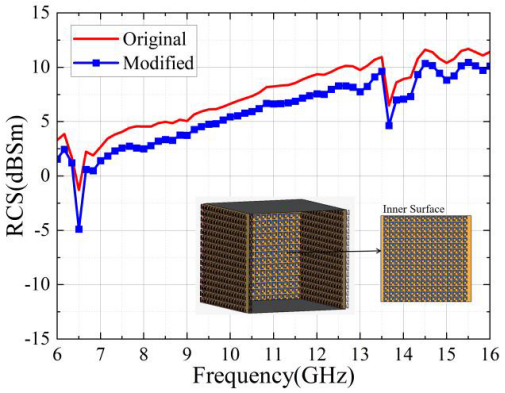

FIGURE 10. RCS comparison of the cavity original and modified manipulation.

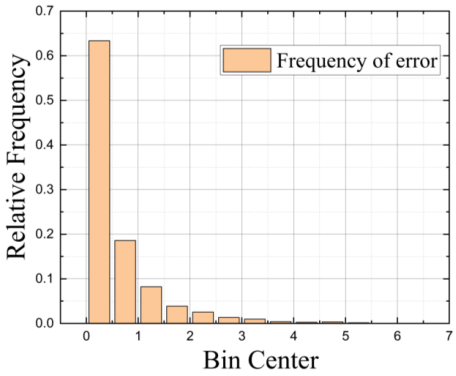

FIGURE 11. Prediction error histogram of the CNN-ResNet Network.

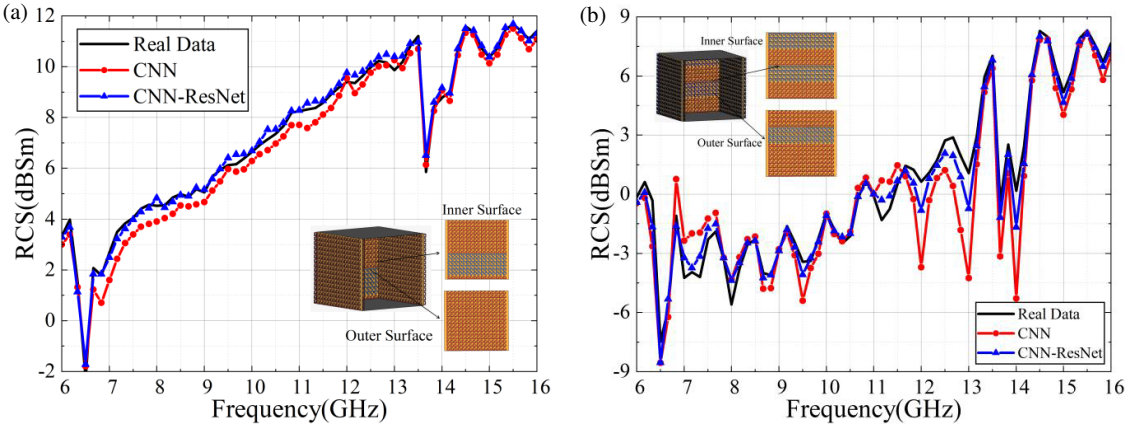

FIGURE 12. Comparison of CNN-ResNet predictions and full-wave algorithm computation results. (a) Configuration 1. (b) Configuration 2.

For this work, a dedicated validation dataset was generated to represent such industrial data. Full-wave simulations were performed using the commercial software FEKO with MLFMM. The frequency range of 6.0–16.0 GHz was sampled at 0.1667 GHz intervals. The dataset comprises 500 training samples. All computations were executed on a Dell Precision 7920 workstation with an Intel Xeon Gold 6248R CPU (3.0 GHz). Each sample required approximately 2.5 hours of computation time, resulting in a total data generation time of approximately 1250 hours.

Figure 11 displays the prediction error distribution. Most errors concentrate near zero, showing a relative frequency of approximately 0.6. The cumulative frequency reaches 0.97 for errors within 3 dB and 0.82 within 1 dB. Error occurrence decreases rapidly with increasing magnitude, with large deviations observed infrequently. This distribution confirms the stability and reliability of the CNN-ResNet framework for phase-to-scattering prediction. The results align consistently with RMSE analysis. This agreement demonstrates the model's robust generalization capability and practical value for metasurface-cavity scattering prediction applications.

To further validate prediction effectiveness, Fig. 11 compares the proposed CNN-ResNet method against a conventional CNN and full-wave simulation results. The metasurface-loaded cavity from Fig. 4 serves as the test structure. Two distinct configurations are examined as shown in Fig. 12(a) and Fig. 12(b). Both employ randomly selected metasurface layouts not included in the original 500-sample training set. Full-wave simulations generate reference RCS data across 6.0–16.0 GHz for both configurations. Comparative predictions are obtained separately using CNN and CNN-ResNet methods. The CNN-ResNet model demonstrates superior accuracy with lower RMSE values. Specifically,as shown in Fig. 12(a), CNN-ResNet method achieves 0.225 dB versus 0.488 dB for conventional CNN. Similarly, as shown in Fig. 12(b), respective values are 0.642 dB and 1.649 dB. All CNN-ResNet predictions maintain errors below 3 dB. This result confirms its effective learning of phase-to-scattering correlations under small-sample conditions. Moreover, as shown in Table 1, under consistent dataset size and splitting ratios with randomly partitioned training/validation sets, both networks were evaluated through 10 independent runs. The CNN achieves an average RMSE of 2.415 dB, while the CNN-ResNet achieves 1.206 dB. These comparative results confirm the superior prediction performance of the proposed method. However, full-wave simulations require mesh regeneration for each geometric variation. They involve constructing and iteratively solving large matrix systems. Computational complexity grows significantly with cavity electrical size. In contrast, the trained CNN-ResNet performs single forward propagation. Computational overhead

becomes negligible compared to full-wave methods. Prediction accuracy remains within practical engineering tolerances. These characteristics simultaneously address the dual demands of computational efficiency and prediction accuracy in engineering design applications.

5. CONCLUSION

This paper proposes a lightweight CNN-ResNet for cavity RCS prediction. This work addresses the practical need for rapid analysis of metasurface-integrated cavity structures. The method overcomes the low computational efficiency of full-wave simulations. The model employs a two-stage framework. Shallow CNNs extract local structural features from phase matrices. ResNet blocks and FC layers then jointly model phase-RCS correlations. This architecture suppresses performance degradation in deep networks. The network was trained on 500 full-wave samples. Each sample contains a 32×48 metasurface array with $0°/180°$ phase states. The model predicts broadband RCS sequences across 6.0–16.0 GHz. Validation shows an RMSE of 1.207 dB. Prediction errors remain below 1.2 dB. Computation time is reduced from hours to milliseconds per sample. This work enables real-time cavity design optimization. The approach achieves an optimal balance between speed and accuracy. It successfully meets engineering demands for both computational efficiency and prediction precision.

ACKNOWLEDGEMENT

This paper is supported by the Opening funding of National Key Laboratory of Digital and Agile Aircraft Design KFJJ-2024-I-02-01-02, National Natural Science Foundation of China U2241203, 62271365.

REFERENCES

[1] Obelleiro-Basteiro, F., J. L. Rodriguez, and R. J. Burkholder, "An iterative physical optics approach for analyzing the electromagnetic scattering by large open-ended cavities," *IEEE Transactions on Antennas and Propagation*, Vol. 43, No. 4, 356–361, Apr. 1995.

[2] Bourlier, C., H. He, J. Chauveau, R. Hémon, and P. Pouliguen, "RCS of large bent waveguide ducts from a modal analysis combined with the Kirchhoff approximation," *Progress In Electromagnetics Research*, Vol. 88, 1–38, 2008.

[3] Lee, C. and S.-W. Lee, "RCS of a coated circular waveguide terminated by a perfect conductor," *IEEE Transactions on Antennas and Propagation*, Vol. 35, No. 4, 391–398, Apr. 1987.

[4] Yang, Y., H. Xin, Y. Liu, H. Cheng, Y. Jin, C. Li, J. Lu, B. Fang, Z. Hong, and X. Jing, "Intelligent metasurfaces: Integration of artificial intelligence technology and metasurfaces," *Chinese Journal of Physics*, Vol. 89, 991–1008, 2024.

[5] Zhao, T., B. Fang, P. Chen, Y. Ke, Z. Kong, C. Shen, C. Li, and X. Jing, "High efficiency flexible control of wave beams based on addition and subtraction operations on all dielectric reflection metasurfaces," *IEEE Sensors Journal*, Vol. 22, No. 5, 4057–4068, Mar. 2022.

[6] Ma, Q., Q. Xiao, Q. R. Hong, X. Gao, V. Galdi, and T. J. Cui, "Digital coding metasurfaces: From theory to applications," *IEEE Antennas and Propagation Magazine*, Vol. 64, No. 4, 96–109, Aug. 2022.

[7] Xu, P., W. X. Jiang, X. Cai, S. H. Bai, and T. J. Cui, "An integrated coding-metasurface-based array antenna," *IEEE Transactions on Antennas and Propagation*, Vol. 68, No. 2, 891–899, Feb. 2020.

[8] Chai, Y., H. Deng, and Q. Xiong, "A dynamically phase tunable metasurface for a broad bandwidth ultra-low radar cross section," *IEEE Access*, Vol. 8, 53 006–53 017, 2020.

[9] Malkiel, I., M. Mrejen, A. Nagler, U. Arieli, L. Wolf, and H. Suchowski, "Plasmonic nanostructure design and characterization via deep learning," *Light: Science & Applications*, Vol. 7, No. 1, 60, 2018.

[10] Paquay, M., J.-C. Iriarte, I. Ederra, R. Gonzalo, and P. d. Maagt, "Thin AMC structure for radar cross-section reduction," *IEEE Transactions on Antennas and Propagation*, Vol. 55, No. 12, 3630–3638, Dec. 2007.

[11] Ameri, E., S. H. Esmaeli, and S. H. Sedighy, "Ultra wideband radar cross section reduction by using polarization conversion metasurfaces," *Scientific Reports*, Vol. 9, No. 1, 478, Jan. 2019.

[12] Pan, Y., F. Lan, Y. Zhang, H. Zeng, L. Wang, T. Song, G. He, and Z. Yang, "Dual-band multifunctional coding metasurface with a mingled anisotropic aperture for polarized manipulation in full space," *Photonics Research*, Vol. 10, No. 2, 416–425, 2022.

[13] Amboli, J., B. Gallas, G. Demésy, and N. Bonod, "Design and analysis of chiral and achiral metasurfaces with the finite element method," *Optics Express*, Vol. 31, No. 26, 43 147–43 162, 2023.

[14] Jia, X., F. Yang, Y. Wen, M. Li, and S. Xu, "Characteristic model and efficient fdtd-spm algorithm for fishnet metasurfaces analysis," *IEEE Transactions on Antennas and Propagation*, Vol. 70, No. 10, 8729–8738, Oct. 2022.

[15] Teng, Y., C. Li, S. Li, Y. Xiao, and L. Jiang, "Efficient design method for terahertz broadband metasurface patterns via deep learning," *Optics & Laser Technology*, Vol. 160, 109058, 2023.

[16] Fu, J., Z. Yang, M. Liu, H. Zhang, and Y. Zhang, "Highly-efficient design method for coding metasurfaces based on deep learning," *Optics Communications*, Vol. 529, 129043, 2023.

[17] Donda, K., Y. Zhu, A. Merkel, S.-W. Fan, L. Cao, S. Wan, and B. Assouar, "Ultrathin acoustic absorbing metasurface based on deep learning approach," *Smart Materials and Structures*, Vol. 30, No. 8, 085003, 2021.

[18] He, Q., H. Chen, Q. Liu, X. Yao, F. Li, D. Liang, J. Xie, and L. Deng, "Ultra-wideband and wide-angle RCS reduction of a concave structure based on a chessboard polarization conversion metasurfaces," *Journal of Physics D: Applied Physics*, Vol. 57, No. 3, 035104, 2023.

[19] He, Q., H. Chen, Q. Liu, X. Yao, F. Li, D. Liang, J. Xie, and L. Deng, "Design of broadband and ultra-wide-angle low-RCS open-ended cavity based on phase cancellation," *International Journal of RF and Microwave Computer-Aided Engineering*, Vol. 2023, No. 1, 9958074, 2023.

[20] Zunair, H. and A. B. Hamza, "Sharp U-Net: Depthwise convolutional network for biomedical image segmentation," *Computers in Biology and Medicine*, Vol. 136, 104699, 2021.

[21] Liu, Z., Y. Lin, Y. Cao, H. Hu, Y. Wei, Z. Zhang, S. Lin, and B. Guo, "Swin transformer: Hierarchical vision transformer using shifted windows," in *2021 IEEE/CVF International Conference on Computer Vision (ICCV)*, 9992–10 002, Montreal, QC, Canada, 2021.

[22] Huang, G., Z. Liu, L. V. D. Maaten, and K. Q. Weinberger, "Densely connected convolutional networks," in *Proceedings of the IEEE Conference on Computer Vision and Pattern Recognition (CVPR)*, 4700–4708, 2017.